Design, assembly, and optical bench testing of a high-numerical-aperture miniature injection-molded objective for fiber-optic confocal reflectance microscopy

Matthew D. Chidley, Kristen D. Carlson, Rebecca R. Richards-Kortum, and Michael R. Descour

The design, analysis, assembly methods, and optical-bench test results for a miniature injection-molded plastic objective lens used in a fiber-optic confocal reflectance microscope are presented. The five-lens plastic objective was tested as a stand-alone optical system before its integration into a confocal microscope for *in vivo* imaging of cells and tissue. Changing the spacing and rotation of the individual optical elements can compensate for fabrication inaccuracies and improve performance. The system performance of the miniature objective lens is measured by use of an industry-accepted slanted-edge modulation transfer function (MTF) metric. An estimated Strehl ratio of 0.61 and a MTF value of 0.66 at the fiber-optic bundle Nyquist frequency have been obtained. The optical bench testing system is configured to permit interactive optical alignment during testing to optimize performance. These results are part of an effort to demonstrate the manufacturability of low-cost, high-performance biomedical optics for high-resolution *in vivo* imaging. Disposable endoscopic microscope objectives could help *in vivo* confocal microscopy technology mature to permit wide-scale clinical screening and detection of early cancers and precancerous lesions.

OCIS codes: 170.1790, 170.2150, 170.3880, 220.3620, 110.4100.

1. Introduction

The optical sectioning ability of confocal microscopy can be exploited to provide dynamic images of human tissue *in vivo* with subcellular resolution at tissue depths up to hundreds of micrometers. Optical sectioning refers to the ability to image a thin slice, at a selected depth, from within a thick specimen by effectively suppressing out-of-focus light.[1] The clinical potential of this technology to aid in the detection and diagnosis of epithelial precancers has been demonstrated.[2–5] We are developing a laser scanning fiber-optic confocal reflectance microscope (FCRM) system for *in vivo* detection of cervical and oral precancers. The general design and operation of this custom microscope system were previously reported.[6,7] This system does not use fluorescent dyes; image contrast is provided by the index mismatch between the nucleus and the cytoplasm of epithelial cells. Preliminary FCRM investigations implemented a commercial microscope objective to develop the basic system and demonstrated imaging at 15 frames/s. To validate the capability for *in vivo* imaging, a 7 mm outer diameter glass-optics miniature microscope objective was successfully designed and implemented on this FCRM. The miniature glass-optics objective interfaced with the FCRM was reported to have a lateral resolution of 2 μm and an axial resolution of 10 μm (FWHM).[8] Clinical cellular images have been obtained *in vivo* with this prototype objective.[9] A detailed description of the design process for this miniature glass-optics objective was also reported.[10]

Continued development of this confocal microscope system is under way to help engineer the technology for large clinical trials. In this paper we report the development of a new prototype plastic miniature objective lens. The main advantage of plastic optics is high-volume fabrication with a significant reduction in unit cost. The objective lens is the only part of the FCRM that physically touches the patient; the rest of the system is connected via a fiber-optic bundle and

M. D. Chidley (mchidley@optics.arizona.edu) and M. R. Descour are with the College of Optical Sciences, University of Arizona, Tucson, Arizona 85721. K. D. Carlson is with the Department of Biomedical Engineering, University of Texas at Austin, Austin, Texas 78712. R. R. Richards-Kortum is with the Department of Bioengineering, Rice University, Houston, Texas 77005.

Received 20 July 2005; revised 14 November 2005; accepted 15 November 2005; posted 17 November 2005 (Doc. ID 63613).

0003-6935/06/112545-10$15.00/0

Table 1. Design Specifications for the BETA Injection-Molded Objective

Specification	Value
NA at object–tissue	1.0 (water immersion)
NA at image–fiber	0.3 (oil immersion)
Working distance (μm)	450
Field of view (diameter, μm)	250
Telecentricity	Object and image space
Wavelength (nm)	1064
Maximum clear aperture (mm)	5
Outer diameter (mm)	7

located on a nearby mobile cart. If the unit cost of the miniature objective can be significantly reduced, this portion of the microscope potentially can be made disposable. Low-cost, single-use probes can help to facilitate large-scale clinical trials of confocal microscopy for precancer detection.

In this paper we present the design, analysis, alignment techniques, and optical bench test results for the injection-molded miniature objective described above. We present the results for the objective as a stand-alone optical system. The total performance achieved when the objective is integrated with the FCRM is significantly reduced by the pixelation from the coherent fiber-optic bundle. Furthermore, the typical refractive index differences in biological tissue range from 0.05 to 0.10,[11] so low levels of light are reflected from human epithelial tissue. Thus it is critical to maximize the optical performance of the miniature objective to prevent any additional loss of resolution or signal.

2. Design Overview

This miniature plastic objective (also identified as the BETA design) is designed to nominally match the specifications of the previous glass-optics prototype described by Liang *et al.*[7] The main BETA optical design specifications are listed in Table 1. Although the functional specifications are almost identical (clear aperture being the only exception), the design process is much different for the current injection-molded prototype than for that which was completed for the glass-optics miniature objective. First, to keep costs reasonable, the glass design included only spherical surfaces, whereas the injection-molded version is free to incorporate aspheric surfaces at no additional cost. During the mold building process, electroless nickel-plated optic inserts are single-point diamond turned for each optical surface. Owing to the inclusion of two aspherical surfaces, the BETA design requires only five lenses, compared with eight lenses for the previous design. The final optical designs for both miniature prototypes are shown in Fig. 1. Even though the clear aperture (CA) for the plastic objective is larger, they both have nominally the same mechanical outside diameter of 7 mm. Both designs are diffraction limited, and each was subjected to a complete tolerance analysis.

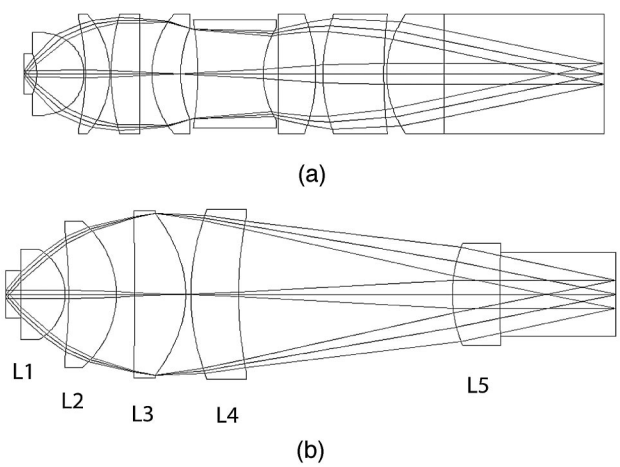

Fig. 1. (a) Optical design layout for the previous eight-element glass-optics miniature objective. The overall object-to-image distance is 20.4 mm and has a maximum CA of 4.2 mm. (b) Current five-element injection-molded plastic (BETA) design layout. Object-to-image distance, 17.9 mm; CA, 5.0 mm.

We used ZEMAX optical design software[12] to design the injection-molded plastic objective. Preliminary designs were created from polystyrene because of its moldability and the availability of its index-of-refraction data (n) in the IR. Eventually Zeonex E48R, a cyclo-olefin polymer, was chosen for its lower moisture absorption and lower inherent birefringence. As previously reported,[13] $n = 1.5200 \pm 0.0005$ ($\pm 2\sigma$) at 1064 nm, and a temperature of 25 °C was experimentally determined and used for this monochromatic optical design. This value agrees with a recently published value to the fourth decimal place.[14]

Compared with the process for a standard glass-optics objective, which is typically housed in a metal barrel, injection molding created new challenges and opportunities. One advantage of injection-molding optics is its ability to directly incorporate the mechanical mounting structure (the flange) with the optical surface, because both can be fabricated at the same time. To facilitate alignment and assembly of the optics, a V-shaped alignment groove, concentric with the optical surface, is included in the flange.[15] The design calls for 500 μm diameter precision balls to be inserted into the groove to properly position the lenses relative to one another. The balls and the V groove allow the optics to be stacked and rotated during assembly of the objective. Figure 2 shows a partially exploded three-dimensional (3D) model of the miniature injection-molded objective. The miniature laser-cut stainless-steel aperture between lenses L3 and L4 identifies the stop location. This is also the location where the compensation (by spacing and rotation) is performed for the experimental results. Other apertures were fabricated in case light scattering from the flange (nonoptical surfaces) should become a problem but currently are deemed unnecessary. The aperture adjacent to lens L5 acts as a baffle to prevent light outside the CA of the rear element from entering the objective during testing. It

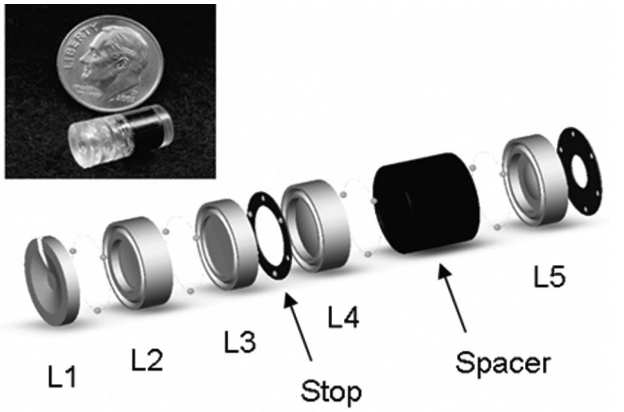

Fig. 2. 3D BETA model; inset, photograph of an actual miniature injection-molded objective.

is slightly oversized to prevent it from becoming the stop surface. The stainless-steel apertures can be coated with a thin layer of flat black paint or chemically blackened. However, for the current tests they were not blackened.

For the design specifications, the diffraction-limited spot size (Airy disk) diameter at the image–fiber side of the objective is 4.3 μm. This value is slightly higher than the average core diameter, 4.1 μm, of the coherent fiber-optic bundle used in the FCRM. To prevent loss of light, the objective needs to be close to diffraction limited. The complete specifications for the coherent fiber-optic bundle are presented in Table 2. The active diameter for the fiber is listed as 1.37 mm, but for the current application a diameter less than 0.830 mm is being used. It should be noted that these fiber-optic bundle specifications differ slightly from those of commercial products currently available from Sumitomo.

3. Optical Analysis and Design Selection

The general tolerances used during the BETA design are listed in Table 3. These tolerances were obtained through discussions with the injection molder. Most of the tolerances employed are classified as either commercial or state of the art for injection-molded plastic optics.[16] Under inspection, indentations were noticed in the V grooves from the 500 μm balls under moderate clamping force. This effect was not modeled in the tolerance analysis, and care must be taken to prevent assembly errors of this type.

A lengthy tolerance analysis helped us find the best compromise among size, expected performance, and cost. The worst tolerances listed in Table 3 are surface wedges in lenses L2 and L3. The compensators used during the tolerance analysis were working distance, object's radius of curvature, and back focal distance. Imaging along a slightly curved object plane in the tissue has produced acceptable results for FCRM systems.[15] The object radius of the final design (1.5 mm) was six times the field-of-view (FOV) diameter, which translates to roughly 5 μm of sag at the edge of the FOV. This amount of sag corresponds to less than a typical epithelial cell diameter. The current tolerance analysis differs from that for a standard glass objective with a single lens cell in that decentration and tilt values must be vector summed. Adjacent lenses must start from the local optical axis of the previous element because of the nature of the mechanical assembly, in which each lens cell is attached to the previous cell at the V groove.

It is well known that plastics experience larger changes in index with temperature than do most glasses.[17] The thermal analysis capabilities of ZEMAX software were used to investigate the robustness of the design to a steady-state temperature change. The maximum temperature change (ΔT) expected during normal use is from room temperature (~20 °C) to body temperature (37 °C) for a $\Delta T = 17$ °C. Allowing the working distance (WD) and the object's curvature to change with the increase in temperature maintains diffraction-limited performance. Because of its unique depth-discrimination properties, the confocal microscope automatically selects the optimum WD and object curvature. In this case, the automatic compensation shifted the WD from 450 to 457 μm and changed the sag at the edge of the field from 5.1 to 5.3 μm. These relatively minor changes are expected to have no effect on the clinical diagnostic capability of the instrument. Tolerance to Δn was examined by iterative stepping of the refractive index away from the design value while the ambient temperature was held constant. The automatic compensation is sufficient to maintain diffraction-limited performance for $\Delta n = \pm 0.005$; by allowing the back focal distance to vary, one can well correct $\Delta n = \pm 0.01$. This tolerance is an order of magnitude larger than any expected Δn.

These analyses provide good confidence in the design's ability to handle the expected manufacturing tolerances, any reasonable steady-state temperature

Table 2. Specifications for the Coherent Fiber-Optic Bundle[a]

Outside diameter (mm)	1.9
Active diameter (mm)	1.37
Number of fibers	30,000
Average fiber core diameter (μm)	4.1
Average center-to-center spacing (μm)	7.1
Nominal NA of fibers	0.3

[a]Sumitomo IGN-15/30 fiber.[6,7]

Table 3. Injection-Molding Manufacturing Tolerances Used for the Tolerance Analysis

Tolerance	Value
Radius (%)	±0.5
Center thickness (μm)	±25
Surface decenter (μm)	±12.5
V-groove decenter (μm)	±5
Element tilt (°)	±0.15
Surface wedge (°)	±0.15
Surface irregularity	3 fringes
Index	±0.001

Table 4. Prescription Data: BETA Miniature Injection-Molded Lens

Surface[a]	Comment	Radius (mm)	Thickness (mm)	Glass ($n_{1064\ nm}$)
Object		1.518	0.45	Seawater (1.3308)
1	L1	100	1.3	E48R (1.520)
2		−1.516	0.1	
3	L2	−16.61	1.4	E48R (1.520)
4		−2.793	0.5368	
5	L3	−100	1.5	E48R (1.520)
6[a]	Stop	−3.130	0.1515	
7[a]	L4	6.549	1.4	E48R (1.520)
8		11.62	6.273	
9	L5	3.836	1.4	E48R (1.520)
10		100	3.389	Index-matching fluid (1.480)
Image		∞		

[a]Aspheric surface.

change, and any other uniform deviation of refractive index from the design value. The final BETA design prescription is provided in Tables 4 and 5.[18]

4. Assembly Methods

To assist assembly, a new as-fabricated design model was created to incorporate any measurable manufacturing errors. Aspheric departure data for surfaces 6 and 7 are included, as well as updated center thicknesses and radii for all lenses. To make the model even more realistic, tilts, decenters, and surface irregularities were incorporated by use of ZEMAX's Monte Carlo (MC) perturbation capabilities. Each MC run consists of 100 random perturbations of the original file. Specifically, the 50% and 90% confidence level results are used as the goal target range of performance during assembly and testing, for which the confidence level indicates the percentage of random perturbations expected to have similar or better performance.

A mechanical fixture (see Fig. 3) was designed to hold the miniature objective during assembly and to provide rotational degrees of freedom during alignment and testing. The fixture consists of four interconnected rings encompassing the miniature objective. The fixture contains set screws to hold the optics in place and slots designed for application of UV curing adhesive (Epotec OG146) with a hypodermic needle. Unfortunately, adhesive applied through the slots tends to cure the optics to the fixture, making them difficult to remove. The usefulness of the current fixture is limited to one rotational degree of freedom and one ball size degree of freedom. Guided by the as-fabricated design model, we decided to fix the lenses on each side of the stop together and allow for rotation only between L3 and L4. Lenses L1–L3 are initially assembled with the help of a miniature mechanical screw press and are UV cured together. Lens L4, the spacer, and lens L5 are then also assembled in the press. The two sections of optics are inserted into their respective parts of the mechanical fixture for testing. The miniature screw press allows for verification that the 500 μm balls properly sit inside their respective V grooves before application of the UV curing adhesive. When the miniature objective is assembled and aligned for testing, the vertical upright end of the mechanical fixture serves as a small water reservoir for the tissue side of the objective.

5. Optical Bench Tests

Optical bench testing analyzes the system performance of the objective before its incorporation into the FCRM. Results for the BETA miniature plastic objective interfaced with the FCRM were recently presented.[19] The results presented here highlight the ball spacing and element rotation method for interactive alignment compensation by use of two injection-molded objectives, labeled BETA15 and BETA17.

A. Performance Metrics

Resolution and modulation transfer function (MTF) testing are used to evaluate system performance.[20] A typical resolution test reports the minimum resolvable bar target on the U.S. Air Force (USAF) standard target when the target is viewed through the objective.[17] This test is subjective; by itself it can be sometimes misleading.[21] The MTF of a system is much more robust, as it provides information over a range of spatial frequencies.

1. Slanted-Edge Modulation Transfer Function Method

With the proliferation of affordable arrayed imaging sensors, a new technique with which to estimate the MTF of an optical system with a single image of a straight edge has recently been accepted. One of the first descriptions of this technique calls it the modified knife-edge technique.[22] It has also been called the angled-edge, tilted-edge, or slanted-edge MTF method.[23–25] This method can be generalized as follows:

(1) Obtain a two-dimensional image of a slightly tilted edge.
(2) Theoretically fit a subpixel line to the edge.

Table 5. BETA Even-Asphere Coefficients[a]

Surface	Conic	4th	6th	8th	10th	12th
6	−1	-2.549×10^{-4}	-1.203×10^{-5}	2.497×10^{-5}	-2.710×10^{-6}	2.167×10^{-7}
7	−1	-1.333×10^{-5}	-8.529×10^{-5}	1.861×10^{-5}	-2.717×10^{-6}	2.264×10^{-7}

[a]Ref. 18.

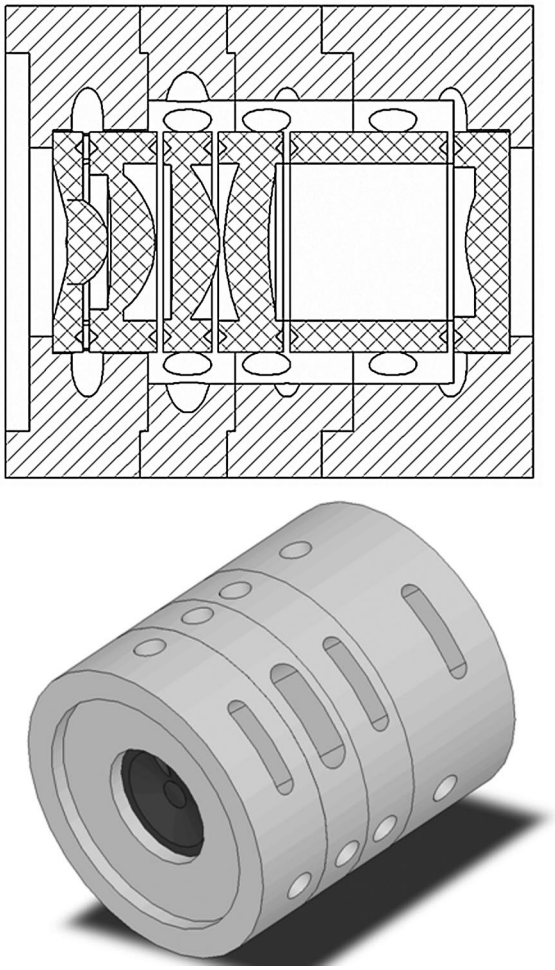

Fig. 3. Cross-sectional drawing and 3D model of a rotation fixture with a miniature objective installed.

(3) Compress the two-dimensional intensity values into a one-dimensional edge-spread function.

(4) Take the derivative of the edge-spread function to get the line-spread function.

(5) Take the Fourier transform of the line-spread function to get the optical transfer function (OTF).

(6) Take the magnitude of the normalized OTF to get the MTF in the direction perpendicular to the edge.

The major distinction among the various methods that estimate the MTF in this way is in the curve fitting method used to fit the edge-spread function data. The International Organization for Standards has adopted one such method for testing digital camera still images, i.e., standard ISO 12233, "Photography—electronic still-picture cameras—Resolution measurements." This standard specifically designates the test as the slanted-edge method and calculates the spatial frequency response of the system. Spatial frequency response is similar to a MTF but is not corrected for the input modulation of the object. Assuming a binary edge transition, however, it is generally accepted that this method provides an estimate of the MTF for a system.[23]

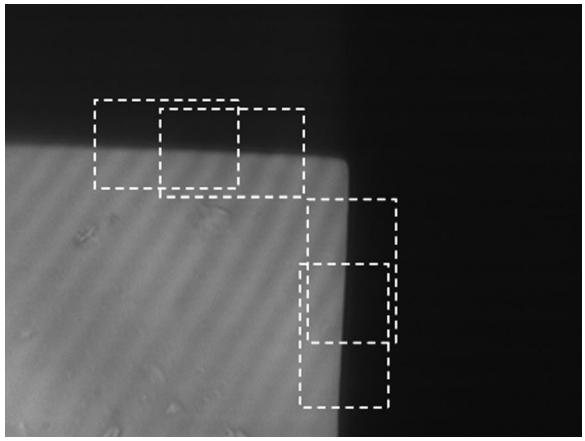

Fig. 4. Four subimages are selected, as shown, from each image. A second image is taken here, and then two images are collected at the opposite corner. A total of 16 subimages from four different edge transitions combines to yield the test MTF curve, which is used to calculate the estimated SR value (BETA17, 700 μm balls from lens L3 to lens L4).

2. Data Sample Selection

As suggested by ISO standard 12233, four images were captured for every test conjugate. The test method samples two subimages for each of two best-focus edges, one horizontal and one vertical, from each image. Figure 4 shows a test image with the nominal locations of the four subimages. Each subimage is 100 × 160 pixels. The total sampled edge length (220–240 pixels) covers approximately 1 μm of sag at the tissue, corresponding to the Rayleigh focus criterion for diffraction-limited performance.[26]

Matlab program sfrmat 2.0 (sfrmat2) follows the essence of ISO standard 12233 and is readily available through the International Imaging Industry Association website.[27] This program has been incorporated into the authors' custom Matlab code, edgeMTF, which has a graphical user interface to facilitate data collection and analysis. The edgeMTF program calculates system magnification, adds the diffraction-limited MTF curve based on the design's NA, and estimates the Strehl ratio. EdgeMTF also has an alignment option to display the Strehl ratio in real time to consistently select best focus edge(s).

3. Estimated Strehl Ratio

There are several common ways with which to compute the Strehl ratio (SR). The method used here is the ratio of areas under the measured and diffraction-limited OTF curves[28]:

$$\mathrm{SR} = \frac{\int\int \mathrm{OTF}_{\mathrm{test}}(\xi,\ \eta)}{\int\int \mathrm{OTF}_{\mathrm{diffraction}}(\xi,\ \eta)}. \qquad (1)$$

Assuming small amounts of aberration, the OTF will remain positive (no contrast reversal), in which case

the MTF equals the OTF and one can estimate the SR from Eq. (1) by replacing the OTF with the MTF. In certain cases, the output from sfrmat2 contains some high-frequency noise that needs to be removed to avoid producing a false increase to the SR estimate. In general, edgeMTF cuts off the data where the MTF first drops below 0.02. Even when the data are thresholded in this manner, there are at least 40 data points from each MTF curve used to calculate the SR.

For our application, performance at a design NA value of 0.3 (in fiber space where the resolution target is placed for the bench-top tests) is the most important criterion. To estimate the SR of the miniature objective under a certain test condition, one divides the test MTF curve by the ideal MTF curve based on the design's NA. The overall system magnification, m_{sys}, is calculated separately for each group of tests and can vary slightly. Any change in system magnification will affect the frequency scaling of the resultant test MTF curve. As the ideal diffraction-limited MTF performance curve remains fixed during testing, these estimated SR values provide the desired relative metric needed during assembly to compensate for best performance. The assumption that the diffraction-limited MTF for all test conditions is equal to the design diffraction-limited MTF is not strictly true because of changes in magnification. However, only a 1%–2% change in the system's magnification is typically observed for the current data, so the assumption of equal diffraction-limited MTFs in the model and the system yields a very good estimate for the SR.

4. Relay Modulation Transfer Function Correction

The initial test MTF curve contains the performance of the entire test system, including the auxiliary relay optics and electronics used to transfer and capture the image from the miniature objective. Typically, when one is testing two high-performance optical systems designed separately, a cascade of geometrical MTFs is a good approximation.[28] By factoring in the change in magnification (test system magnification with and without BETA), one can calculate the MTF for the BETA objective by dividing out the geometrical MTF of the relay optics–electronics. All the results presented have been corrected in this manner.

B. Test Configuration

Figure 5 is a schematic of the test layout used to produce the results presented here. Two lasers are shown in the test configuration. The HeNe visible laser is used for alignment of the test system, and a small Nd:YAG IR laser (Amoco 1064-50P) is used to test at the wavelength of the FCRM system. The IR laser has a fixed output power of 130 mW. A combination of two diffusers, with one of them spinning, is used to eliminate speckle and try to break up the coherence of the light as well as possible. A single diffuser, backilluminated directly with the laser beam, did not efficiently break up the coherence because of the small beam size. The coherent ringing from the edges adversely affected the slanted-edge

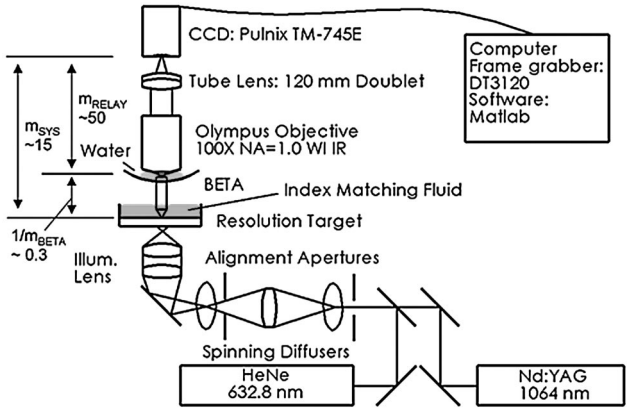

Fig. 5. Optical bench testing diagram.

calculations. The addition of an extra diffuser and lens effectively enlarges the focused spot on the last diffuser, but it also provides redundancy to prevent stoppages during testing. Even with this two-diffuser illumination scheme, faint background interference fringes can be seen in bright areas, thus signifying that the illumination is still partially coherent. The fringes are averaged out in this test method and are not a significant issue. The 0.3 NA side of the test objective was selected to face the resolution target because of the commercial availability of a 1.0 NA water-immersion IR objective (Olympus UM575) that matched the tissue side NA of the miniature objective. The objective is tested backward from the way that it appears in Fig. 1. The rear surface of lens L5 sits in a bath of index-matching fluid (Cargille Laser Liquid 5610), which is designed to prevent Fresnel reflections off the face of the fiber-optic bundle in the FCRM.

Initial alignment of the miniature objective is done with the HeNe laser. Tip, tilt, and x/y translations are performed on the entire objective until the back-reflection from lens L5 is centered on the back of the alignment apertures. Fine adjustments are performed with the IR laser such that maximum light is transmitted to the camera. The commercial objective remains fixed and is not adjusted during testing. This infinity-corrected commercial objective, with a focal length of 1.8 mm in air (or 2.38 mm in water at 1 μm wavelength), is designed to have 100× magnification with a standard tube lens, but the current tests use a 120 mm focal-length doublet as the tube lens. This combination is calculated to have roughly a 50× magnification. The magnification between the object and the CCD is calculated in the software by use of a known bar target spacing and the known camera pixel size. The Matlab image-acquisition toolbox interfaces with a frame grabber (Data Translation DT3120) connected to a monochrome CCD camera with 11 μm × 13 μm pixels (Pulnix TM-745E). Unfortunately, because of slight bleeding in the vertical direction, the MTF for horizontal edges appears less sharp than for vertical edges. The reduced MTF of the CCD in this direction is eventually factored out, as

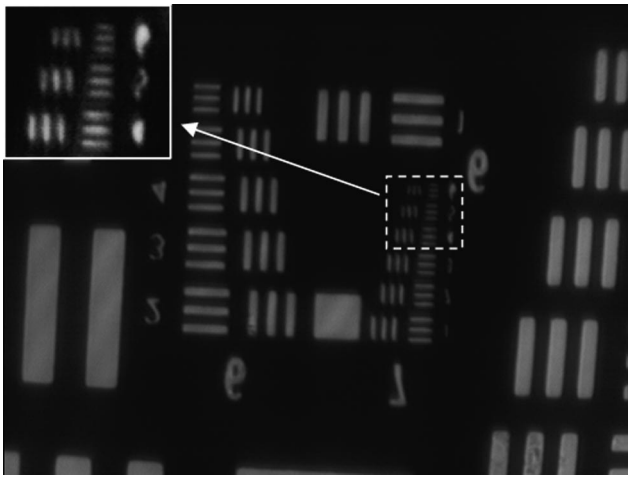

Fig. 6. USAF Test Chart resolution target image obtained with a miniature injection-molded objective (BETA17, 800 μm balls from lens L3 to lens L4). Group 7 element 6 has a spatial frequency of 228 LPMM, corresponding to a resolution of 760 LPMM in tissue space. (The corner inset has been enhanced for display purposes.)

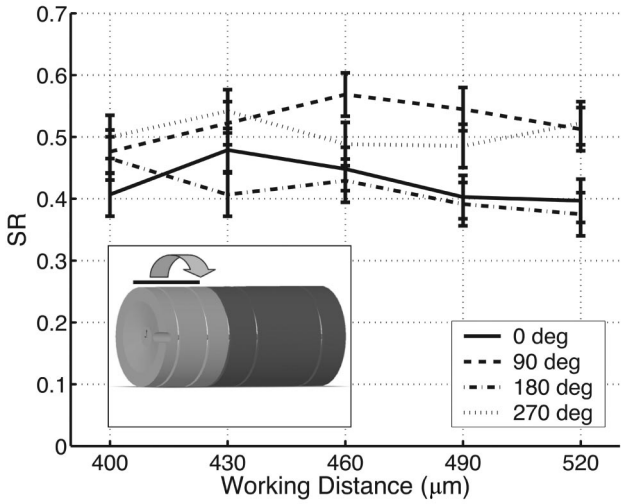

Fig. 7. Estimated SR at multiple conjugates for four rotations (BETA15, 700 μm balls from lens L3 to lens L4).

the MTF of the relay optics–electronics is calculated and stored separately for the vertical and horizontal directions.

C. Results

The BETA optical design uses a slightly curved object surface to take advantage of the confocal microscope's ability to select the best focus surface inside a 3D volume, and thus these optical bench tests, which use a flat object, collect data only over the central portion (~55%) of the FOV. There is no attempt to cover the full FOV because defocus exists for a flat object by design. Defocus at the edges is quite obvious in some images, but, when the object is assembled accurately, the defocus effects do not dominate the image. All MTF plots contain the values obtained for testing the objective at a NA of 0.3 on the fiber side. To convert this value to tissue space, one must multiply the spatial frequency values by the magnification of the BETA objective (~3.3).

1. *Resolution Test*

When the BETA miniature objective is incorporated into the FCRM instrument, it is assumed that the fiber-to-fiber spacing of the fiber-optic bundle [7.1 μm, or 71 line pairs per millmeter (LPMM)] will limit the resolution of the overall system.[8] A sample USAF resolution image obtained with the BETA objective is shown in Fig. 6. The miniature objective can resolve group 7 element 6 (228 LPMM). This objective has an estimated SR of 0.60. When the fiber spacing is demagnified to object space, a lateral sampling of 2.1 μm (240 LPMM) at the tissue is expected for the miniature objective when the objective is attached to the FCRM. When the magnification of the miniature objective is factored in, the group 7 element 6 bar target corresponds to roughly 760 LPMM in tissue space. From these values it is clear that the image resolution of the FCRM will be limited by the fiber-optic bundle.

2. *Rotation and Ball Spacing Compensation*

For this experiment, the bottom two lenses (L4 and L5) remained fixed and the top three lenses (L1–L3) rotated as a single unit. One set of results is shown in Fig. 7. Data are collected for a range of working distances (WDs) nominally centered on the design value of 450 μm. The WD is defined on the water-immersion NA = 1 tissue side. This example shows four rotations being tested. A high level of dependence on the rotational position of the lenses can be observed. Some dependence between the 180° spaced data sets is observed; both the 0° and 180° rotations perform noticeably worse than the 90° and 270° positions. From the as-fabricated design model it was expected that rotational alignment would play a less significant role in compensation of performance. Because of the unexpectedly large dependence of performance on the rotation of the lenses, this experiment was repeated with other BETA objectives. Similar results were obtained.

Changing the ball size between the third and fourth lenses is also investigated. Data are collected over a range of ball sizes from 500 to 900 μm, and the maximum SR for each ball size is shown in Fig. 8. The ZEMAX as-fabricated (As Fab) model data come from MC simulations with 100 random perturbations for each of the five ball sizes. The MC 50% and MC 90% confidence-level files are selected, and the MTF curves are used to calculate the estimated SR values that are shown in Fig. 8.

A relative error analysis for the SR values was calculated to be $\Delta SR = \pm 0.01$ ($\pm 2\sigma$). This value factors in changes of magnification and random sources of error. During testing, the magnification is held constant across a range of conjugates, but in reality there is a small change in magnification. The random sources of error are assumed to include noise and

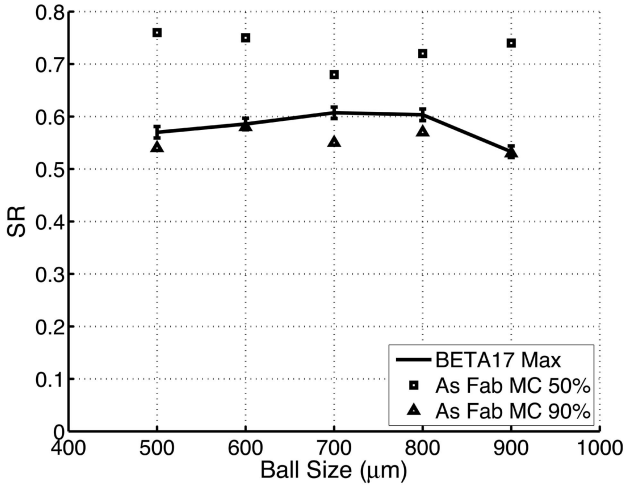

Fig. 8. Estimated SR maxima for different-sized balls from lens L3 to lens L4 while the same rotational alignment (BETA17) is maintained.

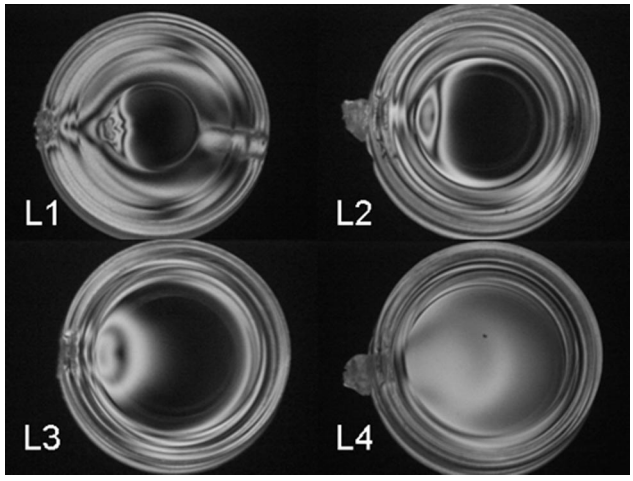

Fig. 9. BETA gray-scale birefringence images (light source–left-hand circular polarizer–lens–right-hand circular polarizer–microscope–camera).

focus repeatability. The random component of the uncertainty is reduced as the square root of N, the number of subimage samples. The two individual components are combined by use of the root-sum-squares method. This idealized uncertainty calculation is most appropriate for best-case data points selected from a larger group of data, as in Fig. 8. There are other possible sources of error in the data, but these are not so easily quantifiable. From a limited amount of rotation repeatability data, $\Delta SR = \pm 0.035$ was observed owing to alignment tilt issues with the rotation fixture. This value is used for the error bars in Fig. 7.

3. *Results and Discussion*

The reasons for these large variations in performance with angular position are not fully understood, but two main sources have been identified: alignment tilt and birefringence. The large range of ball sizes caused some alignment tilt issues each time the rotation fixture was rotated. The evidence for flow-induced birefringence is based on observation of the individual lenses between polarizers. Four of the five BETA lenses have significant amounts of birefringence; see Fig. 9. Lens 5 seems to be exempt from these problems and is not shown. The birefringence is typically localized to the area around the injection gate. These birefringence patterns are consistent for each lens over the short prototype molding run.

The best performance level obtained thus far corresponds to an estimated SR of 0.61. The combined MTF curve for this data point is shown in Fig. 10 and represents the average of 16 subimages taken from 4 separate images. The analysis evenly weights the performance from four different edge transitions. The four main edges are dark-to-bright and bright-to-dark transitions for both horizontal and vertical edges. Inclusion of data from all four edges is of extreme importance when one is comparing relative performance among optical systems that exhibit non-rotationally symmetric errors. To better illustrate this conclusion with the current example, we give the four subimage averages, one for each edge transition: $SR_{V1} = 0.73$, $SR_{V2} = 0.65$, $SR_{H1} = 0.70$, $SR_{H2} = 0.36$.

Obviously, the SR average value of 0.61 could have been much higher if not for the second horizontal edge measurements. Caution must be exerted to ensure that the overall performance of these objectives not be judged or compared without a complete set of edge orientations.

The as-fabricated model data represent an average of on-axis and four off-axis fields [$(\pm 52.8\ \mu m, 0)$ and $(0, \pm 52.8\ \mu m)$ in object–tissue space]. The distances were selected to match the experimental testing conditions. The on-axis data were weighted by a factor of 4 to yield an average that evenly considers on- and off-axis performance. The as-fabricated model provides an estimate based on the manufacturing tolerances discussed above and does not currently account for any of the observed birefringence effects. The es-

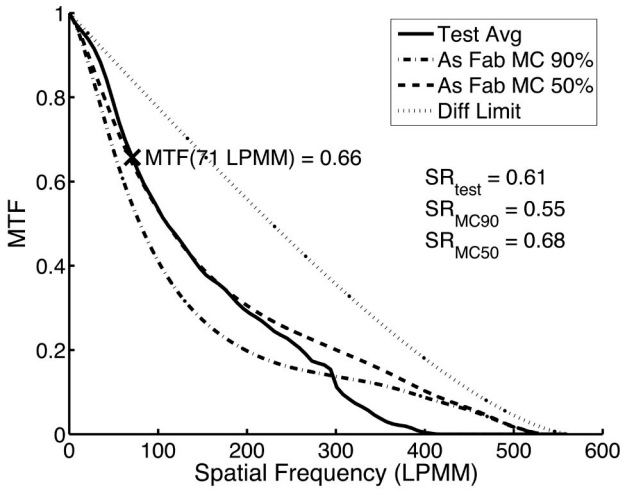

Fig. 10. Combined test MTF (BETA17, 700 μm balls from lens L3 to lens L4) with as-fabricated ZEMAX model data.

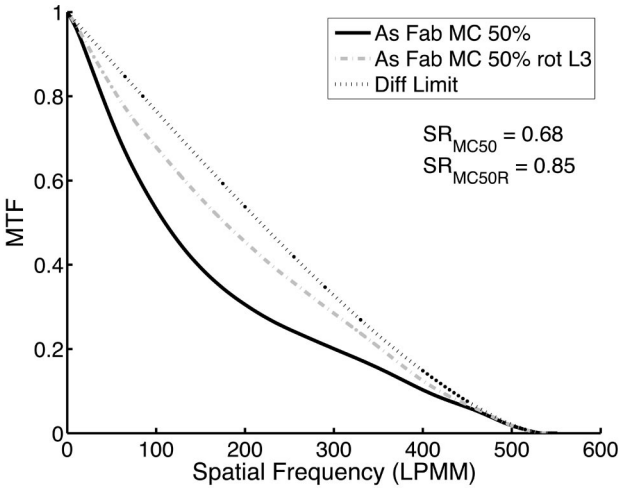

Fig. 11. Effect of rotation of lens L3 on as-fabricated ZEMAX model.

timated performance uses object curvature, working distance, and image focus as compensators. Figure 11 considers rotation of lens L3 as an additional compensator. In this figure the MC 50% file considered in Fig. 10 is reoptimized with rotation about the optical axis for lens L3 as a variable. This significant improvement is noticed only in roughly half of MC files.

The results presented help to unravel the difficulties of building high-NA miniature plastic optics. Currently the three main factors that can degrade the optical performance of the BETA miniature injection-molded plastic objective are (1) alignment methods and optomechanical design, (2) birefringence, and (3) microscratches on lens L1.

We expect that, owing to new birefringence constraints, the second injection-molded prototype objective will cost slightly more than the first; however, this additional cost does not detract from the large price reduction possible for a commercial production run. The scratches on the second surface of lens L1 may have been incurred during the handling and shipping of the lenses and could be prevented with a better optomechanical design that does not leave any surface unprotected. In addition, a better optomechanical design can also help to reduce the assembly time and permit better control during alignment.

6. Final Comments

Our first prototype of a miniature injection-molded plastic objective for fiber confocal reflectance microscopy has been presented. Features specific to the design, tolerance analysis, and testing of this miniature injection-molded plastic objective have been discussed. The goal of this investigation into high-NA plastic optics is to determine the feasibility of high-volume disposable FCRM optical probes. One major benefit already realized is that aspheric surfaces have allowed a reduction to five elements, compared with eight in the previous all-glass-optics prototype objectives. With this benefit comes the challenge of developing a robust optical alignment method that allows the same level of control to be exerted as traditional optical mounting and assembly techniques. While alignment of the device remains a challenge, the results presented here provide insight into the design, manufacturing, and alignment of future-generation high-NA plastic objectives. Miniaturization compounded with testing a dual immersion objective is also challenging. Consequently, an elaborate test setup has been constructed and a customized Matlab optical testing program based on the slanted edge MTF method has been written. The best performance obtained to date is an estimated Strehl ratio of 0.61 with a modulation of 0.66 at the fiber-optic bundle Nyquist sampling limit. It has been demonstrated that rotational alignment of lens groups is currently critical to optical performance.

Editing and review of this manuscript by University of Arizona research professor Tomasz Tkaczyk is gratefully acknowledged. This research was funded by the National Cancer Institute under grant R01-CA73920 and follow-on grant R01-CA82880, both titled “Fiber-Optic, *In Vivo* Confocal Microscopy.” This paper contains selections of text from the dissertation titled “High numerical aperture injection-molded miniature objective for fiber-optic confocal reflectance microscopy,” submitted by M. Chidley in partial fulfillment of the requirements for the Ph.D. degree at the University of Arizona.

References and Notes

1. T. Wilson, “Confocal microscopy,” in *Biomedical Photonics Handbook,* T. Vo-Dinh, ed. (CRC Press, 2003), pp. 10-2–10-4.
2. T. Collier, A. Lacy, A. Malpica, M. Follen, and R. Richards-Kortum, “Near real-time confocal microscopy of amelanotic tissue: detection of dysplasia in *ex vivo* cervical tissue,” Acad. Radiol. **9,** 504–512 (2002).
3. M. Rajadhyaksha, R. R. Anderson, and R. H. Webb, “Video-rate confocal scanning laser microscope for imaging human tissues *in vivo,*” Appl. Opt. **38,** 2105–2115 (1999).
4. W. Zheng, M. Harris, K. W. Kho, P. S. Thong, A. Hibbs, M. Olivo, and K. C. Soo, “Confocal endomicroscopic imaging of normal and neoplastic human tongue tissue using ALA-induced-PPIX fluorescence: a preliminary study,” Oncol. Rep. **12,** 397–401 (2004).
5. A. F. Gmitro and D. Aziz, “Confocal microscopy through a fiber-optic imaging bundle,” Opt. Lett. **44,** 565–567 (1993).
6. K. B. Sung, C. Liang, M. R. Descour, T. Collier, M. Follen, A. Malpica, and R. Richards-Kortum, “Near real time *in-vivo* fibre optic confocal microscopy: sub-cellular structure resolved,” J. Microsc. **207,** 137–145 (2002).
7. C. Liang, M. R. Descour, K. B. Sung, and R. Richards-Kortum, “Fiber confocal reflectance microscope (FCRM) for *in vivo* imaging,” Opt. Express **9,** 821–830 (2001).
8. K. B. Sung, C. Liang, M. R. Descour, T. Collier, M. Follen, and R. Richards-Kortum, “Fiber optic confocal reflectance microscope with miniature objective for *in vivo* imaging of human tissues,” IEEE Trans. Biomed. Eng. **49,** 1168–1172 (2002).
9. K. Sung, R. Richards-Kortum, M. Follen, A. Malpica, C. Liang, and M. R. Descour, “Fiber optic confocal reflectance microscopy: a new real-time technique to view nuclear morphology in cervical squamous epithelium *in vivo,*” Opt. Express **11,** 3171–3181 (2003).

10. C. Liang, K. B. Sung, R. Richards-Kortum, and M. R. Descour, "Design of high NA miniature objective for endoscopic fiber confocal reflectance microscope (FCRM)," Appl. Opt. **41,** 4603–4610 (2002).
11. A. K. Dunn, C. Smithpeter, A. J. Welch, and R. Richards-Kortum, "Sources of contrast in confocal reflectance imaging," Appl. Opt. **35,** 3441–3446 (1996).
12. ZEMAX Development Corporation, http://www.zemax.com/.
13. M. D. Chidley, C. Liang, M. Descour, K. B. Sung, R. Richards-Kortum, and A. Gillenwater, "Miniature injection-molded optics for fiber-optic, *in vivo* confocal microscopy," in *International Optical Design Conference*, P. K. Manhart and J. M. Sasian, eds., Proc. SPIE **4832,** 126–136 (2002).
14. N. G. Sultanova, I. D. Nikolov, and C. D. Ivanov, "Measuring the refractometric characteristics of optical plastics," Opt. Quantum Electron. **35,** 21–34 (2003).
15. C. Liang, "Design of miniature microscope objective optics for biomedical imaging," Ph.D. dissertation (University of Arizona, 2002).
16. S. Baumer, *Handbook of Plastic Optics* (Wiley-VCH, 2005), p. 28.
17. R. E. Fisher and B. Tadic-Galeb, *Optical System Design* (McGraw-Hill, 2000), pp. 110 and 302–307.
18. Source, ZEMAX *Optical Design Program User's Guide* (February 2005), p. 243.
19. K. Carlson, M. D. Chidley, K. B. Sung, M. R. Descour, A. Gillenwater, M. Follen, and R. Richards-Kortum, "*In vivo* fiber-optic confocal reflectance microscope with an injection-molded plastic miniature objective lens," Appl. Opt. **44,** 1792–1797 (2005).
20. W. J. Smith, *Modern Optical Engineering,* 3rd ed. (McGraw-Hill, 2000), pp. 366–377.
21. B. Wells, "Test and measurement: MTF provides an image-quality metric," Laser Focus World, **41**(10), S7± (2005).
22. A. P. Tzannes and J. M. Mooney, "Measurement of the modulation transfer function of infrared cameras," Opt. Eng. **34,** 1808–1817 (1995).
23. P. D. Burns, "Slanted-edge MTF for digital camera and scanner analysis," in *PICS 2000: Image Processing, Image Quality, Image Capture, Systems Conference* (The Society for Imaging Science and Technology, 2000), pp. 135–138.
24. P. D. Burns and D. Williams, "Refined slanted-edge measurements for practical camera and scanner testing," in *PICS 2002: Image Processing, Image Quality, Image Capture, Systems Conference* (The Society for Imaging Science and Technology, 2002), pp. 191–195.
25. P. B. Greer and T. van Doorn, "Evaluation of an algorithm for the assessment of the MTF using an edge method," Med. Phys. **27,** 2048–2059 (2000).
26. J. E. Greivenkamp, *Field Guide to Geometrical Optics* (SPIE Press, 2004), p. 89.
27. International Imaging Industry Association: http://www.i3a.org/downloads_iso.html.
28. G. D. Boreman, *Modulation Transfer Function in Optical and Electro-Optical Systems* (SPIE Press, 2001), pp. 28 and 85–88.